Science Advances

AAAS

Supplementary Materials for

Artificial visual systems enabled by quasi–two-dimensional electron gases in oxide superlattice nanowires

You Meng, Fangzhou Li, Changyong Lan, Xiuming Bu, Xiaolin Kang, Renjie Wei, SenPo Yip, Dapan Li, Fei Wang, Tsunaki Takahashi, Takuro Hosomi, Kazuki Nagashima, Takeshi Yanagida, Johnny C. Ho*

*Corresponding author. Email: johnnyho@cityu.edu.hk

The PDF file includes:

Supplementary Texts S1 to S5
Figs. S1 to S22
Tables S1 to S3
Legend for movie S1
References

Other Supplementary Material for this manuscript includes the following:

(available at advances.sciencemag.org/cgi/content/full/6/46/eabc6389/DC1)

Movie S1

Supplementary Text 1

An control experiment about thermal heating-induced water molecules desorption is carried out to exclude the possibility of water molecules adsorbed onto NW surface layers acting as the charge trapping sites (Fig. S6). Electrical characteristics of passivation-free devices are measured and compared at both room temperature and 150 °C. Even though thermal heating is utilized to remove the adsorbed water molecules here, there are not any distinct changes when comparing the device transfer and output characteristics (Fig. S6). This result may exclude the possibility of water molecules adsorbed onto NW surface layers acting as the charge trapping sites (*47*). It is as well consistent with the charge trapping model reported in the literature. In specific, the adsorbed water molecules usually behave as electron donors, whereas the adsorbed oxygen species act as acceptor-like trapping sites (*48-50*). Thus, in this work, the desorption of oxygen molecules from the NW surface is inferred to release the trapped electrons participating in the carrier transport, resulting in the enhanced conductivity of $InGaO_3(ZnO)_3$ superlattice NWs in vacuum.

Supplementary Text 2

In this work, the energy consumption for a single spike event is defined as the sum of electrical energy consumption (E_1) and input light energy consumption (E_2). Electrical energy consumption can be calculated from the equation, $E_1 = I_{peak} \times t \times V$, where I_{peak} is the peak value of EPSC for a single spike event, t is the spike duration, and V is the applied bias voltage. Input light energy consumption is calculated from the equation, $E_2 = P \times A \times t$, where P is the input light intensity and A is the effective irradiated area on the NWs. Here, we use the cross-sectional area ($A = n \times L \times D$; n is the number of nanowires in the device channel, L is the channel length, d is the nanowire diameter) to estimate the effective irradiated area of the nanwoires. As a result, for a particular case (*i.e.,* bias voltage~0.1 mV, t_{spike}~10 ms, light density~0.01 mW/cm^2), the energy dissipation of single spike event is estimated to be ~0.7 fJ. Scaling down the device dimensions and reducing the spike durations to sub-millisecond levels could be utilized as feasible strategies to futher decrease the energy consumption per event.

Supplementary Text 3

Generally, the generated photocurrent (I_{ph}) depends on the incident light intensity (P) and follows the power law dependence ($I_{ph} \sim P^{\alpha}$). The power exponent α is usually less than 1, resulting from the complex processes of electron-hole generation, trapping, and recombination, which is typically observed for semiconducting materials. In principle, if photodetectors can be incorporated with memory devices, they should also enable high-performance ultra-weak light detection by long-term accumulation of optical signals. This way, the charge storage accumulative effect would become domain for traditional photodetectors, exhibiting an exponential-association photoelectric conversion law of ($I_{ph} \sim a \cdot (1 - e^{-b \cdot P \cdot t})$). Under this condition, more charge carriers can be accumulated in the NWs through the longer light exposure and thus giving rise to the higher responsivities and detectivities of photodetectors. Significantly, with a duration time of 1000 ms, quasi-2DEGs photonic synapses exhibit a high responsivity of 1.05×10^6 A/W and a high detectivity of 3.15×10^{13} Jones (Fig. S8). All these performance parameters are already comparable to those state-of-the-art low-dimensional semiconductor-based photodetectors (Table S2).

Supplementary Text 4

To better understand the device operation mechanism, simplified schematic diagrams are utilized and illustrated in Fig. 2j, in which oxygen adsorption-induced charge trapping and subsequent optically-induced charge release are highlighted. In the dark, oxygen molecules (O_2) adsorbed onto NW surfaces become negatively charged ions (O^{2-}) by capturing free electrons from the superlattice NW cores: $O_2(g) + e^- \rightarrow O_2^-(ad)$. These adsorbed oxygen would deplete the $InGaO_3(ZnO)_3$ NW and make it yielding the relatively low conductivity. Based on the photogating effects, since the trapped carriers on NW surfaces have a certain spatial distribution, they induce an additional electrostatic field to modulate the channel conductance. Upon exposure to UV light, the photo-generated holes migrate to the NW surface and discharge the adsorbed oxygen ions through surface electron-hole recombination: $h^+ + O^{2-}(ad) \rightarrow O_2(g)$. At the same time, the photo-generated electrons get collected by the multiple quantum wells, and hence significantly increase the conductivity of quasi-2DEGs. When the UV irradiation is turned off, the photoexcited states are spatially separated due to the potential barriers existed between InO_2^- layers and $GaO(ZnO)_3^+$ blocks. These heterointerface barriers then prevent the reversed diffusion of electrons from superlattice NW core to NW surface (*51*). The localized electrons in superlattice NW cores would lead to a long tail in the relaxation process, giving rise to the synaptic plasticity in quasi-2DEGs photonic synapses.

Supplementary Text 5

Utilizing the biological transmitter release model proposed by Magleby (*38*), each pulse during repetitive stimulation is assumed to contribute a residual facilitation, f(t), whose magnitude and time scheduling are identical. This way, the experimental residual facilitation can be compiled as a function of time (nΔt) after single light pulse stimulation as depicted Fig. S17a. It is noted that Δt is the interval time (500 ms) between two sequential pulses. Clearly, the residual facilitation of the quasi-2DEGs photonic synapse fits well with the stretched-exponential relaxation law. With the aim to make the analysis more explicitly, the residual facilitation is normalized. These residual facilitatory effects are expected to add up linearly to get the total facilitation, F(t), during repetitive stimulation. The experimental results of the quasi-2DEGs photonic synapse during repetitive stimulation were shown in Fig. S17b. Indeed, the total facilitation at a given time is the total of the residual facilitation contributed by each impulse before that time. The total facilitation after the time of nΔt, F(nΔt), can be formalized to,

$$F(n\Delta t) = \sum_{k=1}^{n} f(k\Delta t)$$

where f(kΔt) is the residual facilitation at the time of nΔt. As each facilitation after the pulse stimulation follows the same relaxation law, given as F(t), it is possible to estimate the facilitation contributed by a single pulse during repetitive stimulation such that,

$$f(n\Delta t) = F(n\Delta t) - F\big((n-1)\Delta T\big)$$

where f(nΔt) is the residual facilitation contributed by the first pulse in the repetitive stimulation train at the time of nΔt, and F(nΔt) - F((n - 1)Δt) is the difference of total facilitation between the time of nΔt and the time of (n - 1)Δt. For example, the relationship of f(3Δt) = F(3Δt) - F(2Δt) is observed in Fig. S17a. This proves the validity of the biological transmitter release model to distinguish the continuously programed conductance states in the quasi-2DEGs photonic synapses. All these results and analysis verify again the feasibility of using quasi-2DEGs photonic synapses to emulate brain-like learning and memory functions.
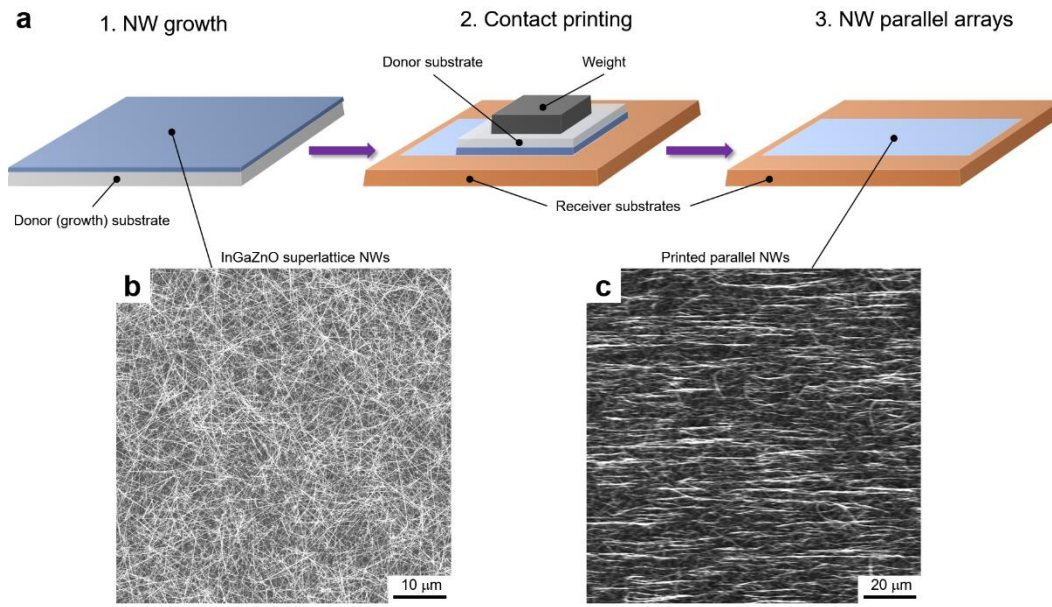
Fig. S1. Contact printing of InGaZnO superlattice NWs. (a) Schematic illustration of NW contact printing process used in this work. SEM images of (b) InGaZnO superlattice NWs on the growth substrate and (c) printed NW parallel arrays on the receiver substrate.
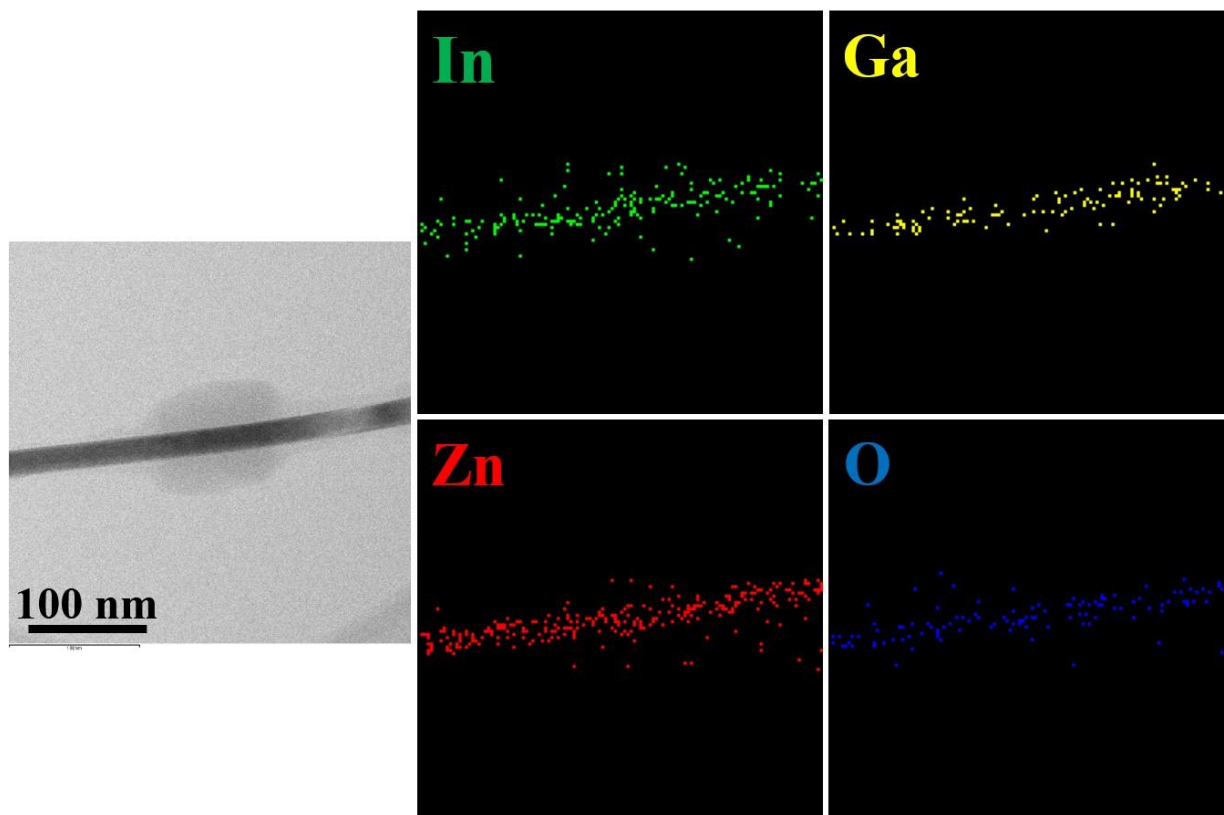
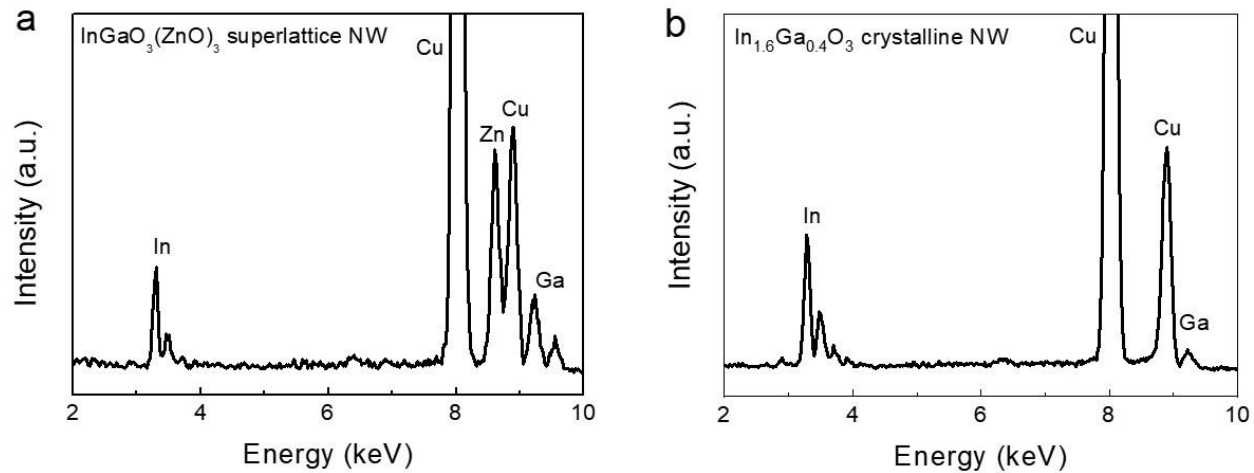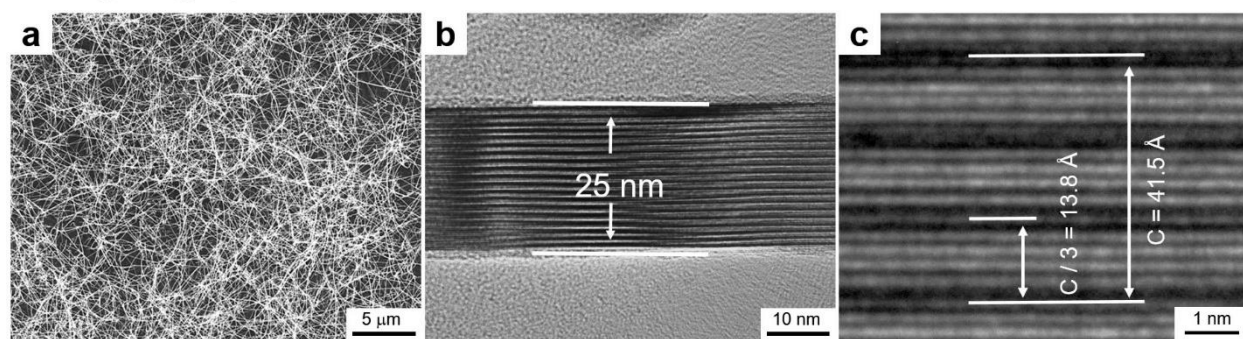**Fig. S2.** EDS elemental mappings of a representative $InGaO_3(ZnO)_3$ superlattice NW.

Fig. S3. EDS spectra of (a) a typical $InGaO_3(ZnO)_3$ superlattice NW and (b) a typical $In_{1.6}Ga_{0.4}O_3$ crystalline NW.

InGaO$_3$(ZnO)$_3$ superlattice NW

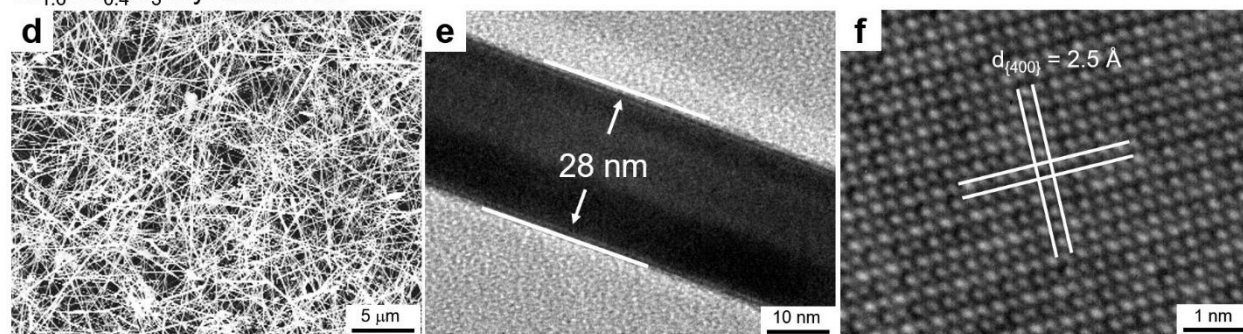InGa$_{1.6}$Ga$_{0.4}$O$_3$ crystalline NW

Fig. S4. Microstructural comparisons between InGaO$_3$(ZnO)$_3$ superlattice NWs and crystalline In$_{1.6}$Ga$_{0.4}$O$_3$ NWs. (a) SEM image and (b, c) HRTEM images of InGaO$_3$(ZnO)$_3$ superlattice NWs. (d) SEM image and (e, f) HRTEM images of In$_{1.6}$Ga$_{0.4}$O$_3$ crystalline NWs.
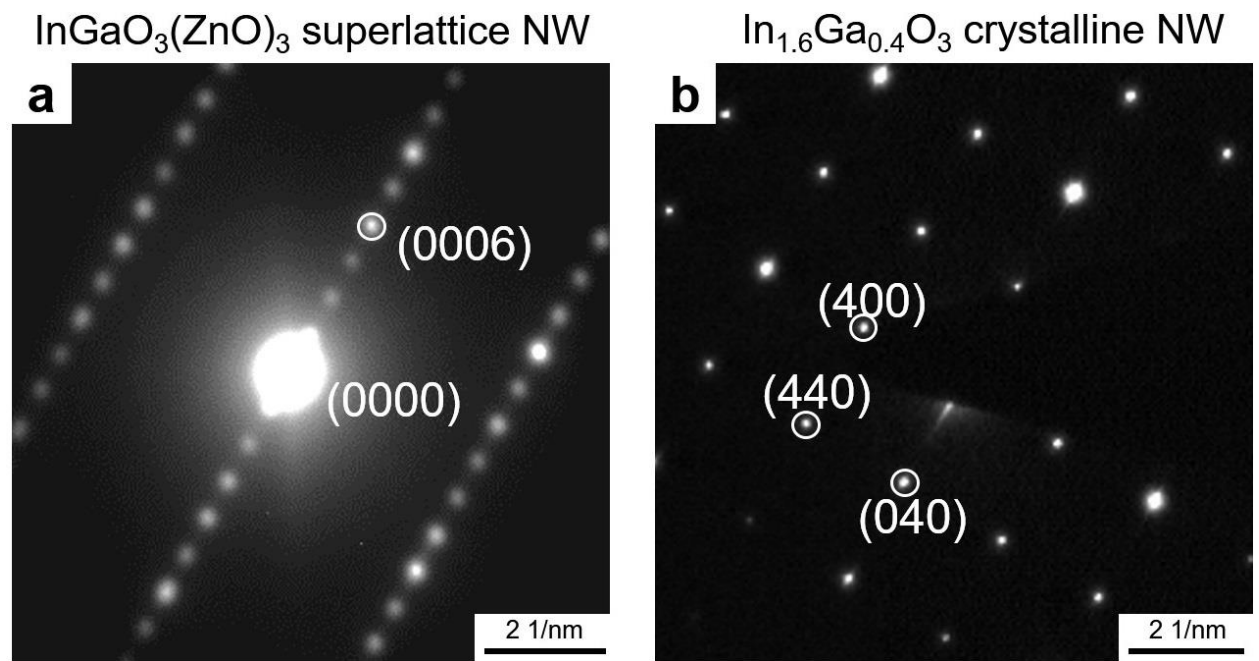
InGaO$_3$(ZnO)$_3$ superlattice NW   In$_{1.6}$Ga$_{0.4}$O$_3$ crystalline NW

Fig. S5. SAED patterns of (a) a typical InGaO$_3$(ZnO)$_3$ superlattice NW and (b) a typical In$_{1.6}$Ga$_{0.4}$O$_3$ crystalline NW.
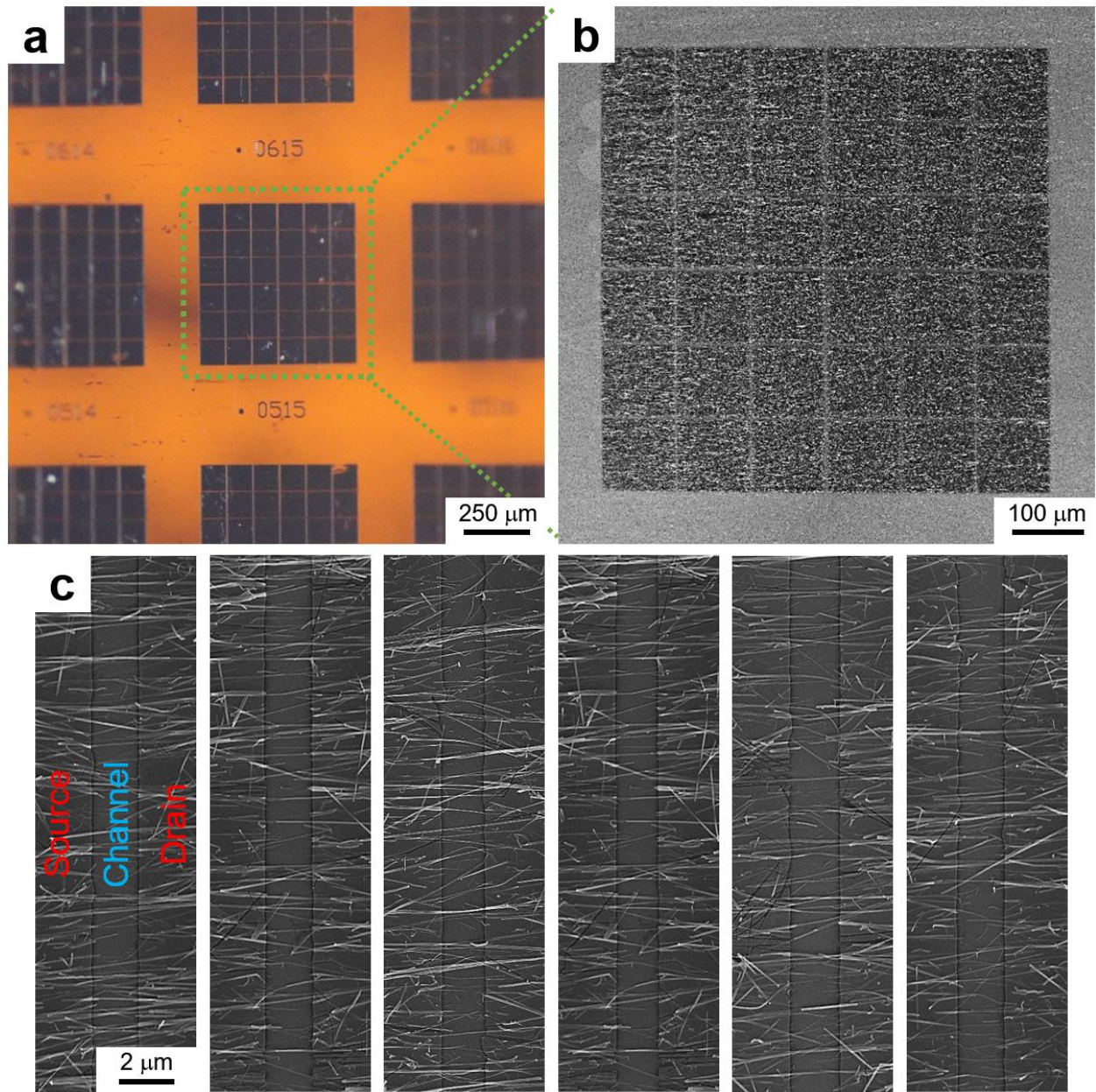
Fig. S6. Quasi-2DEGs photonic synapse arrays with uniform NW distribution. (a) Microscope and (b) SEM images of the artificial visual system based on quasi-2DEGs photonic synapse device arrays (6×5 array). (b) Typical SEM images of the individual device channel regions.
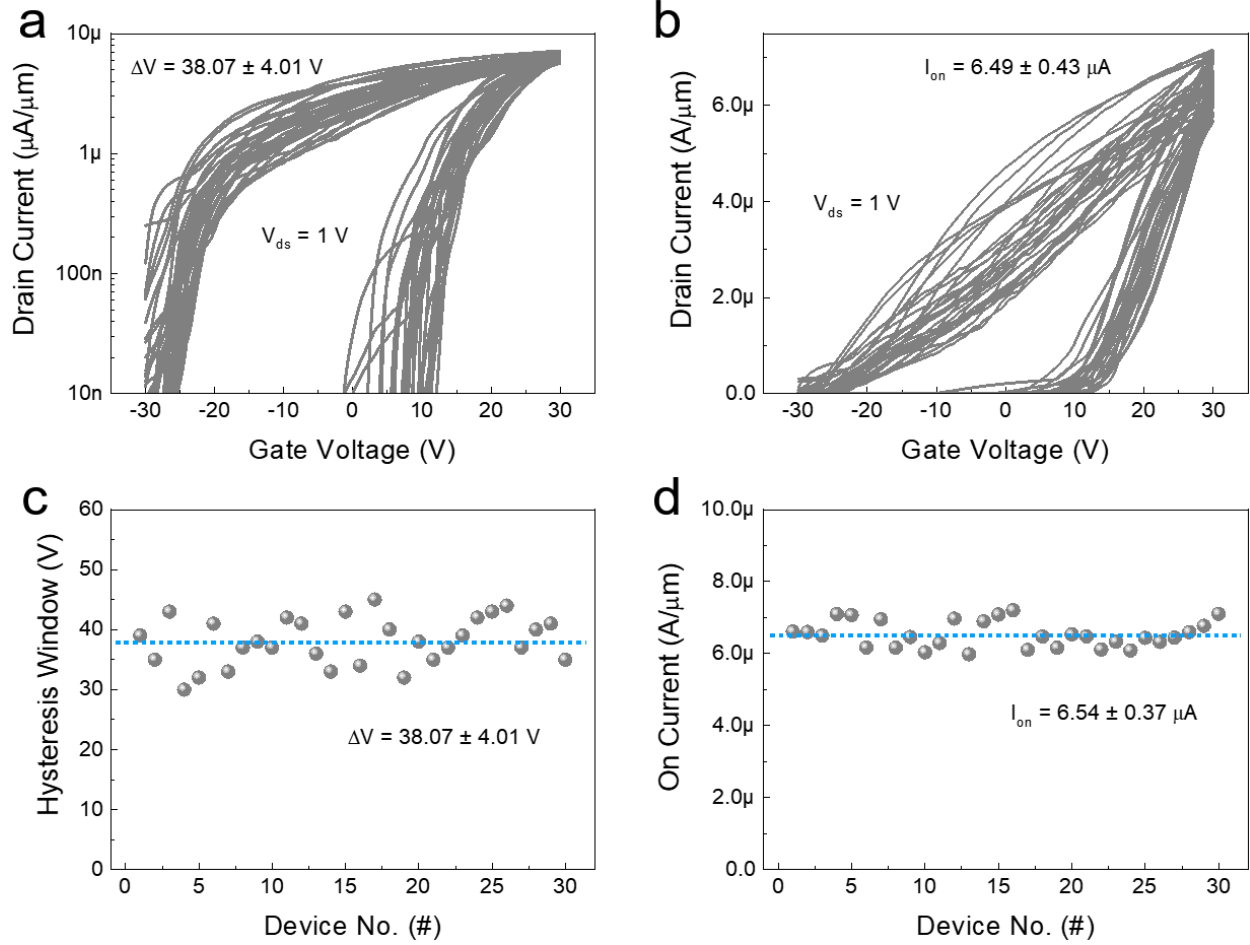
Fig. S7. Quasi-2DEGs photonic synapse arrays with uniform device performance. (a) Transfer characteristics of different $InGaO_3(ZnO)_3$ NW array devices in the 6×5 array using (a) logarithm y-coordinate and (b) linear y-coordinate. Statistics of the hysteresis window and on current of 30 different $InGaO_3(ZnO)_3$ NW array devices.

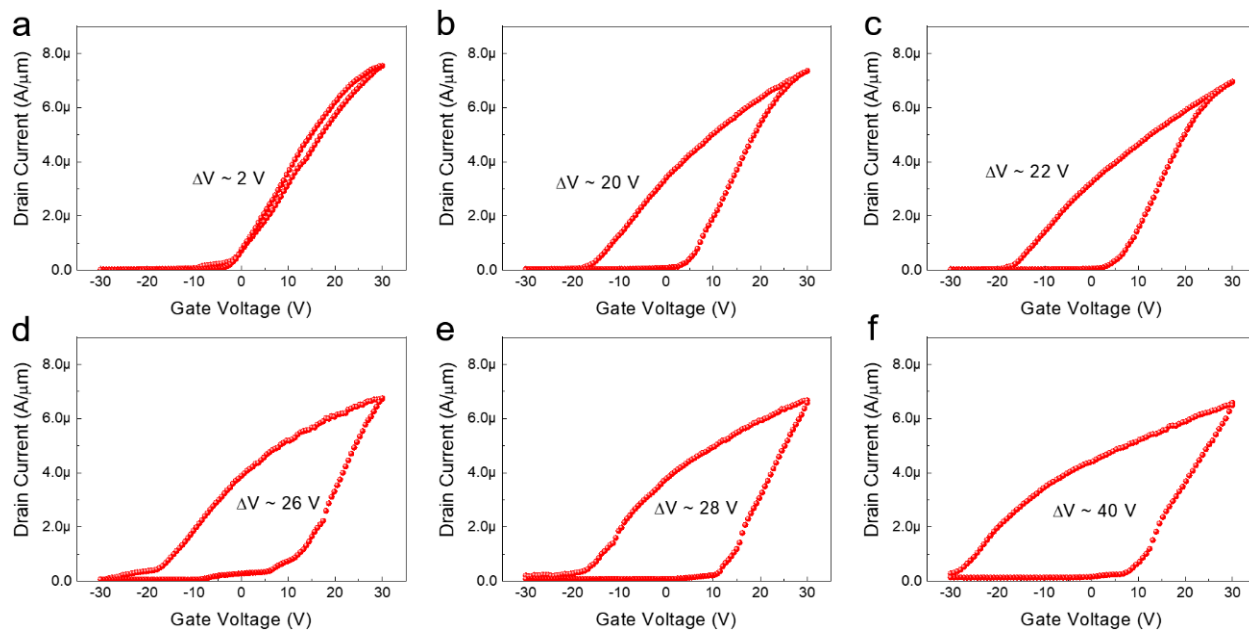**Fig. S8.** Hysteresis and recovery characteristics of InGaO$_3$(ZnO)$_3$ superlattice NW FETs. (a-f) Transfer characteristics of InGaO$_3$(ZnO)$_3$ superlattice NW FETs with different exposing time of 0, 1, 2, 3, 5 and 12 hours, respectively, after the storage in vacuum for 48 hours.
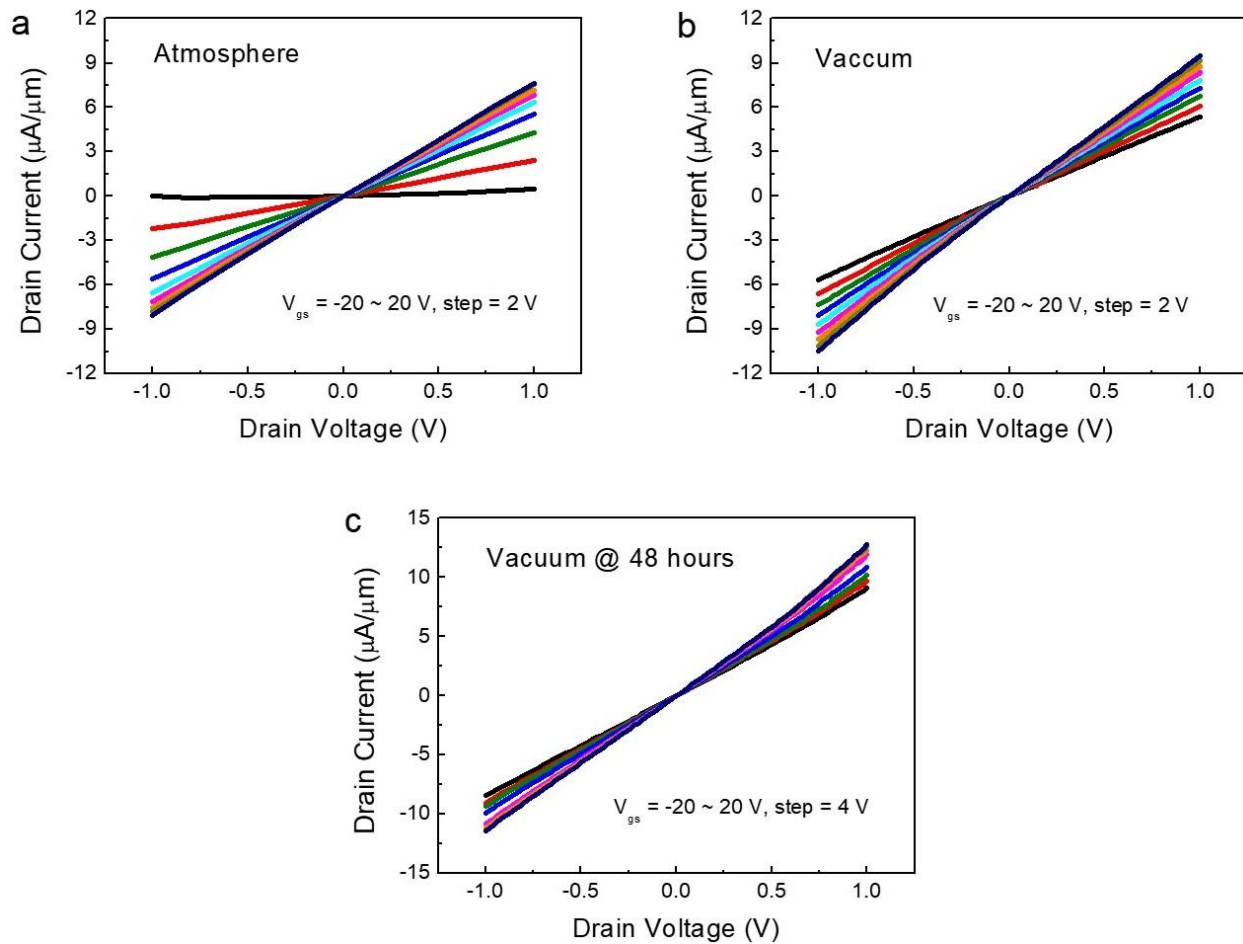
Fig. S9. Output characteristics of a representative InGaO$_3$(ZnO)$_3$ superlattice NW array FET (a) measured at ambient atmosphere, (b) measured at vacuum condition immediately, and (c) measured after 48-hour vacuum storage.
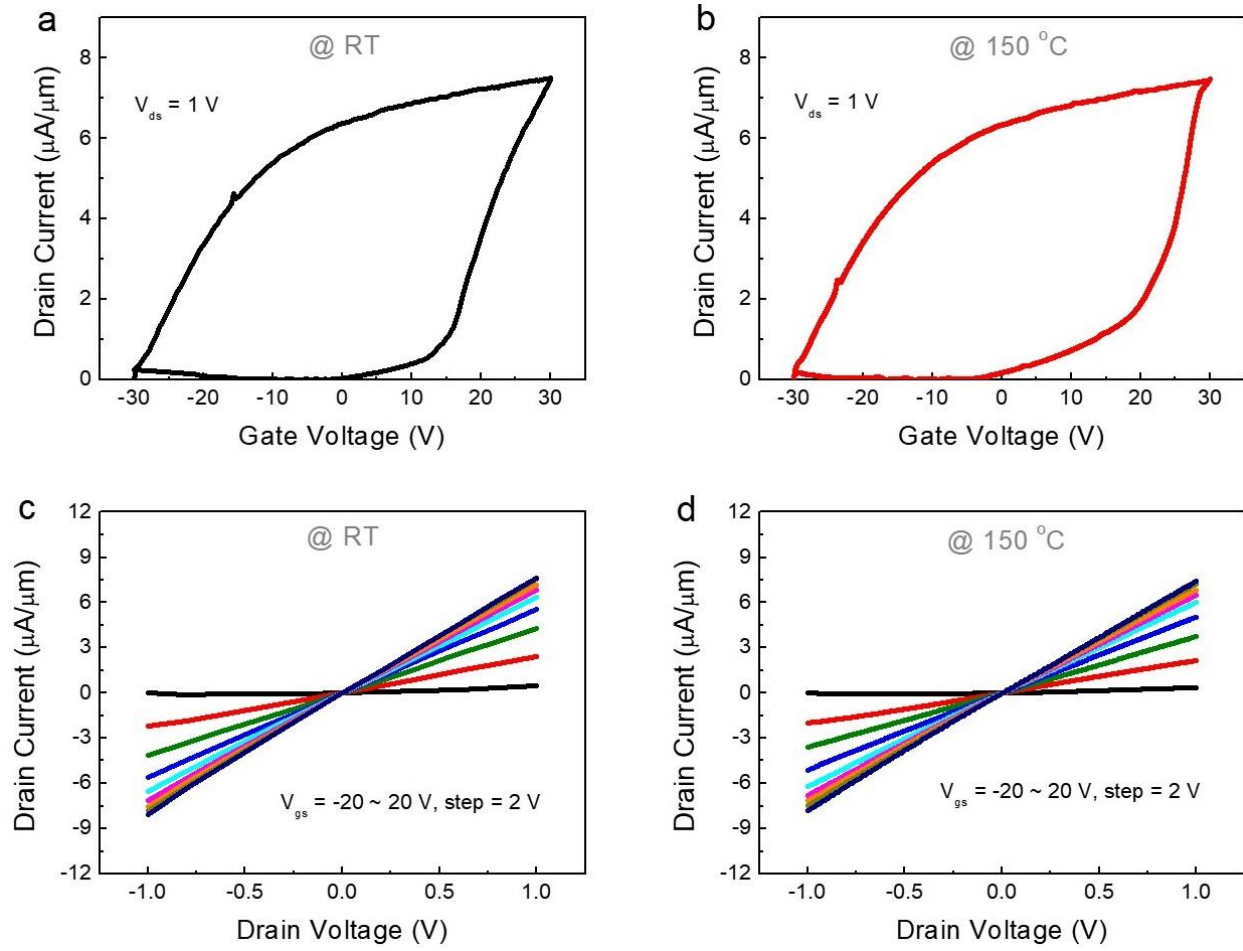
Fig. S10. Transfer characteristics and output characteristics of $InGaO_3(ZnO)_3$ superlattice NW array FET measured at (a, c) room temperature and at (b, d) 150 °C.
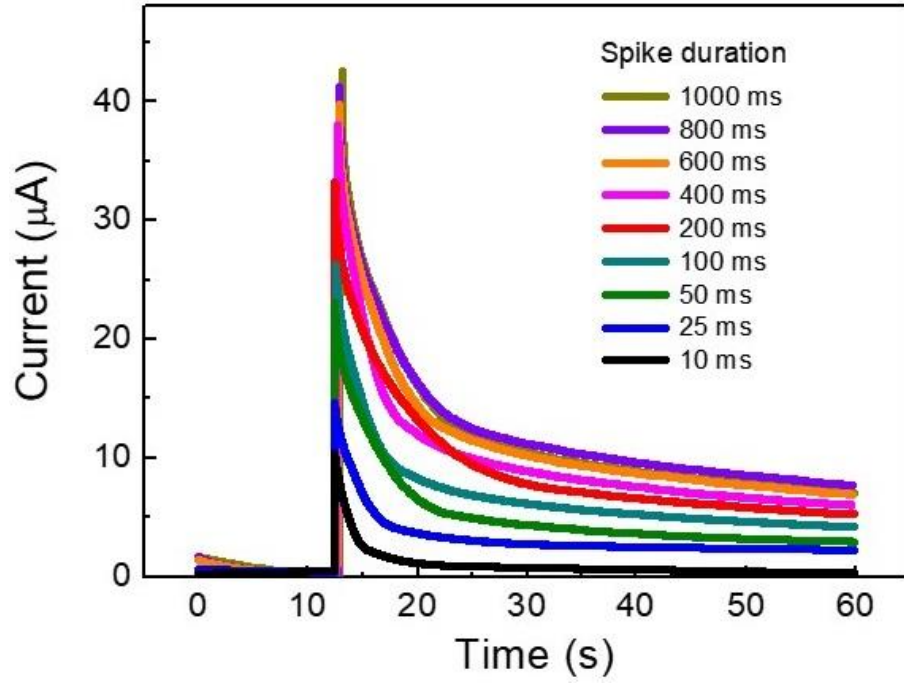
Fig. S11. Light spike-induced EPSC generation and decaying characteristics of $InGaO_3(ZnO)_3$ superlattice NW arrays with spike time sapnning from 10 ms to 1,000 ms.

Fig. S12. Responsivity and detectivity of $InGaO_3(ZnO)_3$ superlattice NW arrays at different spike duration time spanning from 10 ms to 1,000 ms.
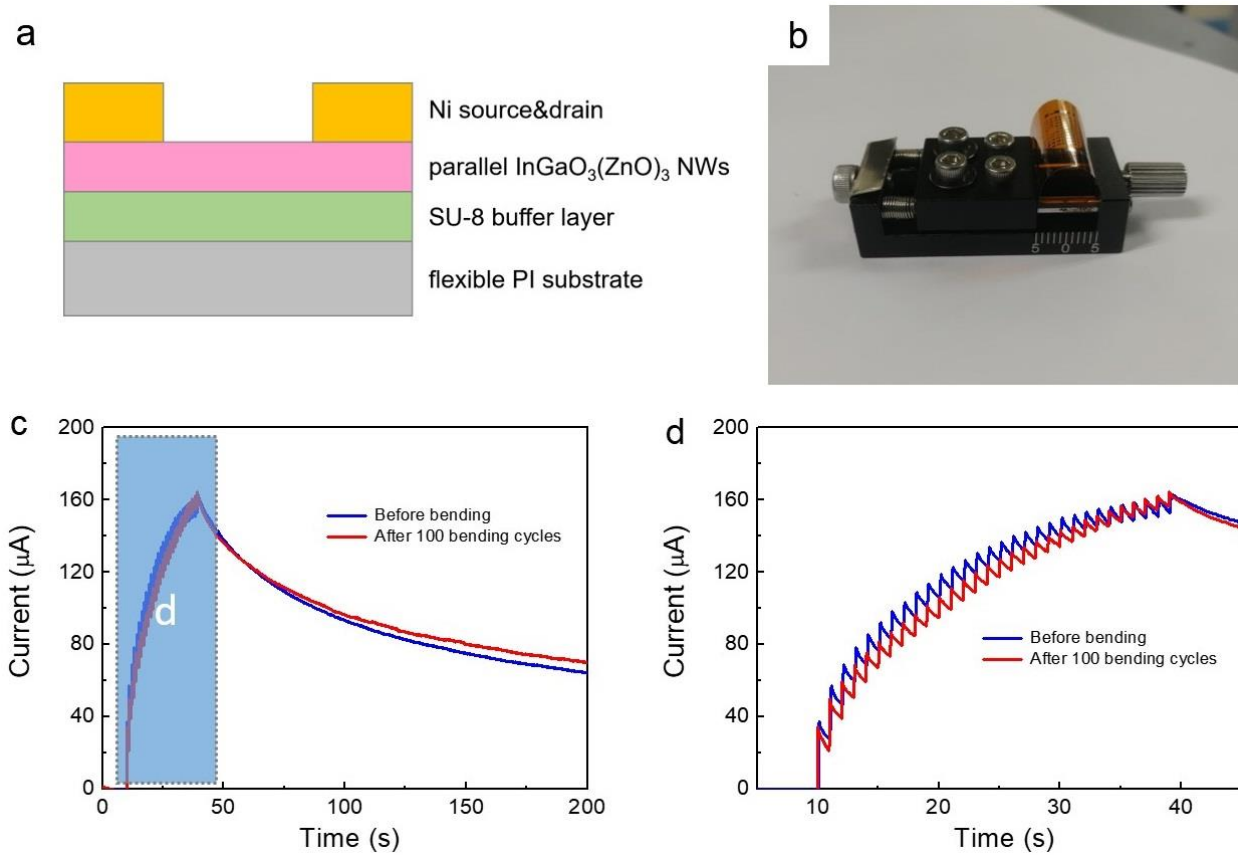
Fig. S13. Flexible quasi-2DEGs photonic synapses. (a) Schematic structure of flexible quasi-2DEGs photonic synapses on polyimide (PI) substrate. (b) Photograph of bending test setup with a bending radius of ~0.5 mm. Photo Credit: You Meng, City University of Hong Kong. (c) and (d) electrical measurements of flexible quasi-2DEGs photonic synapses before and after 100 successive bending cycles.
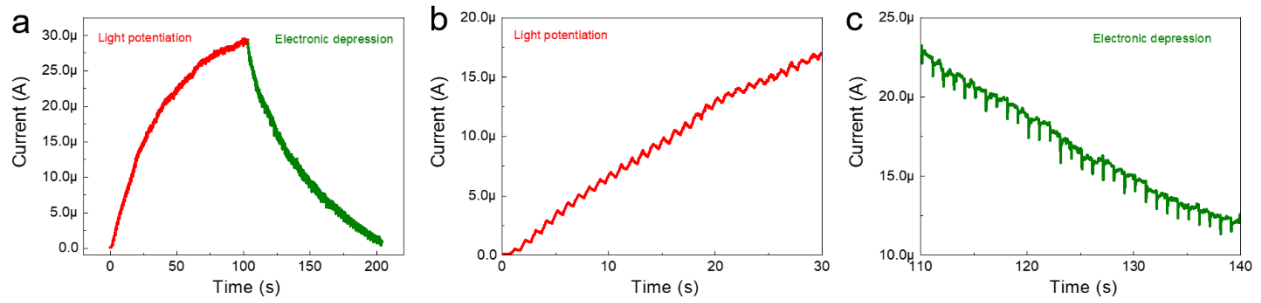
Fig. S14. Dynamic potentiation/suppression behaviors of quasi-2DEGs synapses. (a) Potentiation and suppression behaviors caused by the sequential 100 photonic pulses (0.05 mW/cm^2 amplitude, 10 ms duration, 1 s interval) and sequential 100 negative electric pulses (-5 V amplitude, 10 ms duration, 1 s interval). Figures (b) and (c) show the localized regions in Figure (a).
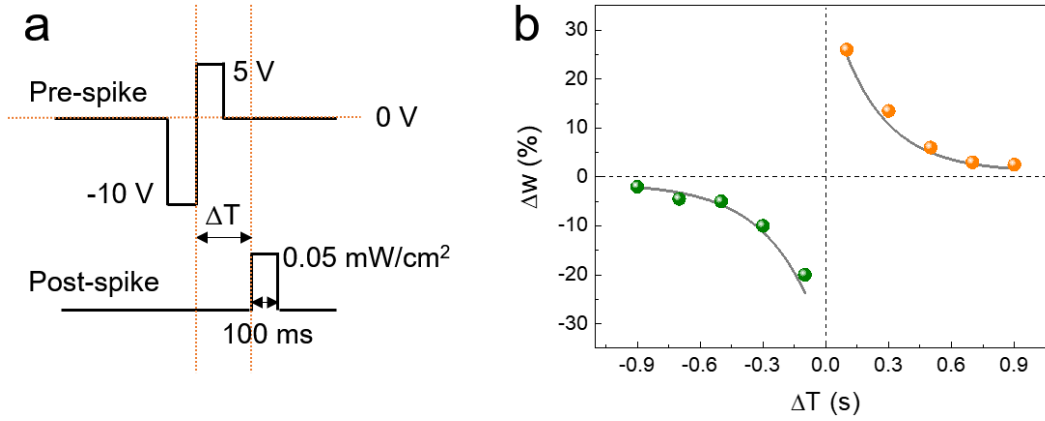
Fig. S15. STDP behaviors of quasi-2DEGs synapses. (a) Pre- and post-synaptic spikes used in the Hebbian STDP measurements. (b) Asymmetric Hebbian learning STDP behaviors of the quasi-2DEGs synapses. The relative change in conductivity represents the variation of synaptic weight (ΔW). The spike interval time (ΔT), defined as $T_{post-spike} - T_{pre-spike}$, is ranging from 100 ms to 900 ms.
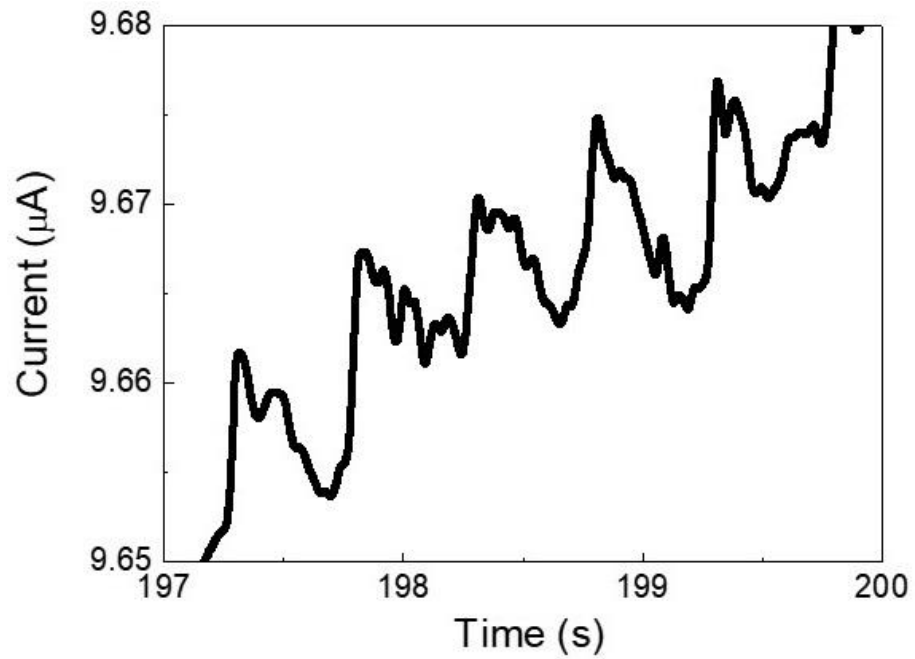
Fig. S16. Multi-bit storage properties of flexible InGaO$_3$(ZnO)$_3$ superlattice NW arrays.
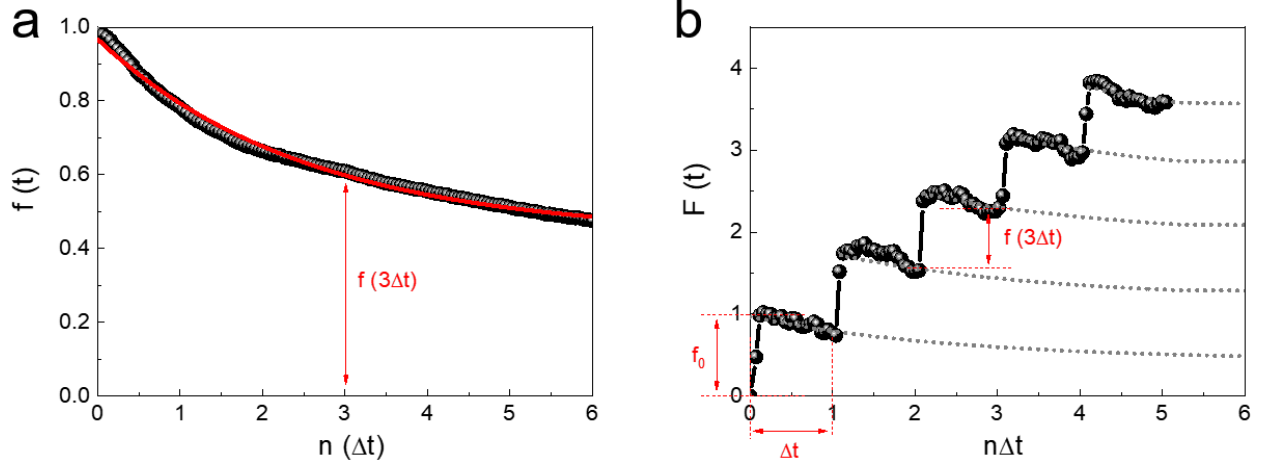
Fig. S17. Facilitation behaviors of quasi-2DEGs photonic synapses based on the biological transmitter release model. (a) Normalized residual facilitation, f(t), as a function of time. Time is expressed as $n\Delta t$, where Δt is the interval time (500 ms) between two sequential pulses. The red line is the fitted curve based on the stretched-exponential relaxation law. (b) Total facilitation, F(t), as a function of time during repetitive stimulation. The dashed lines are the fitted curves based on the transmitter release model in biological synapses.
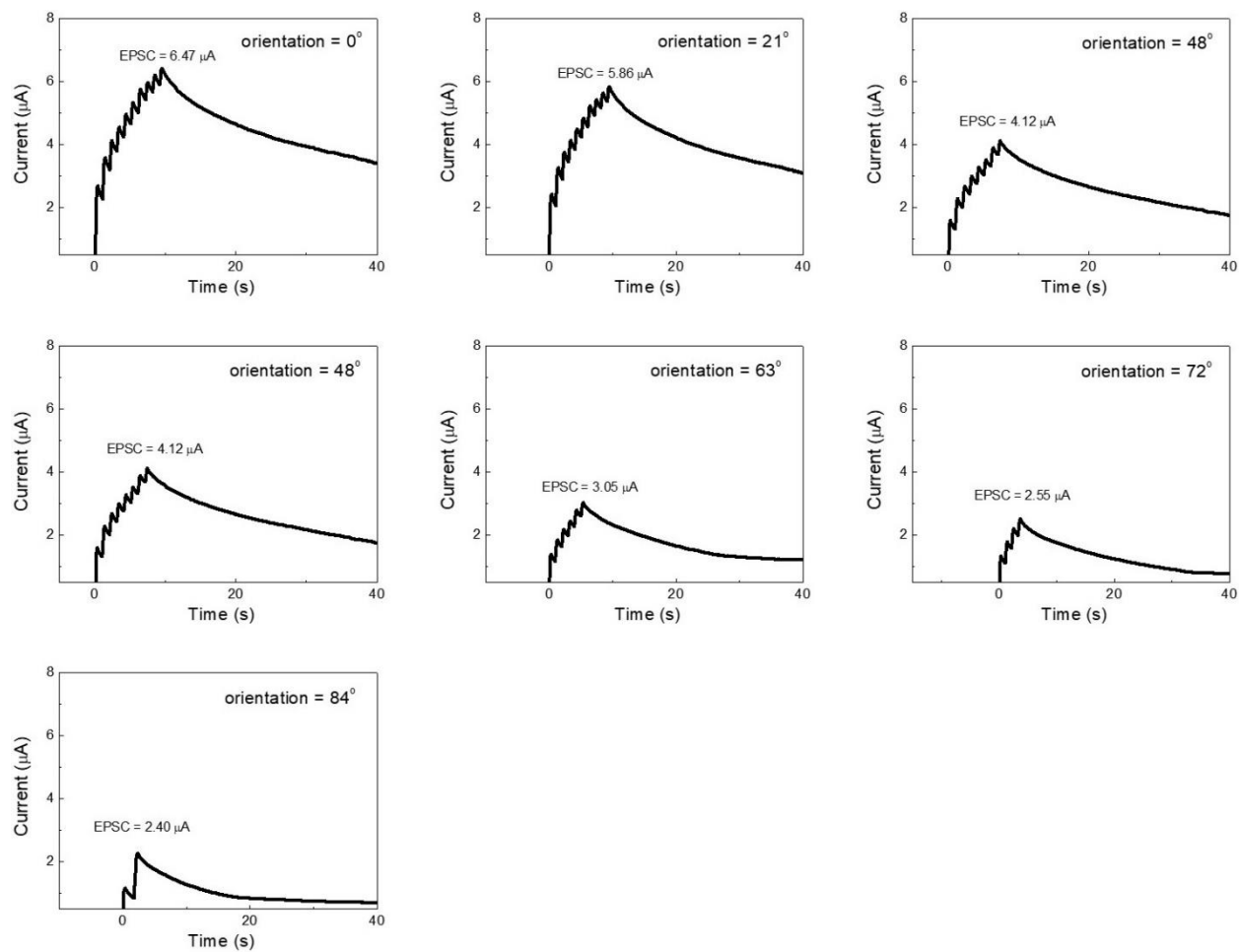
Fig. S18. Visual responses of quasi-2DEGs photonic synapses with different orientation angles.
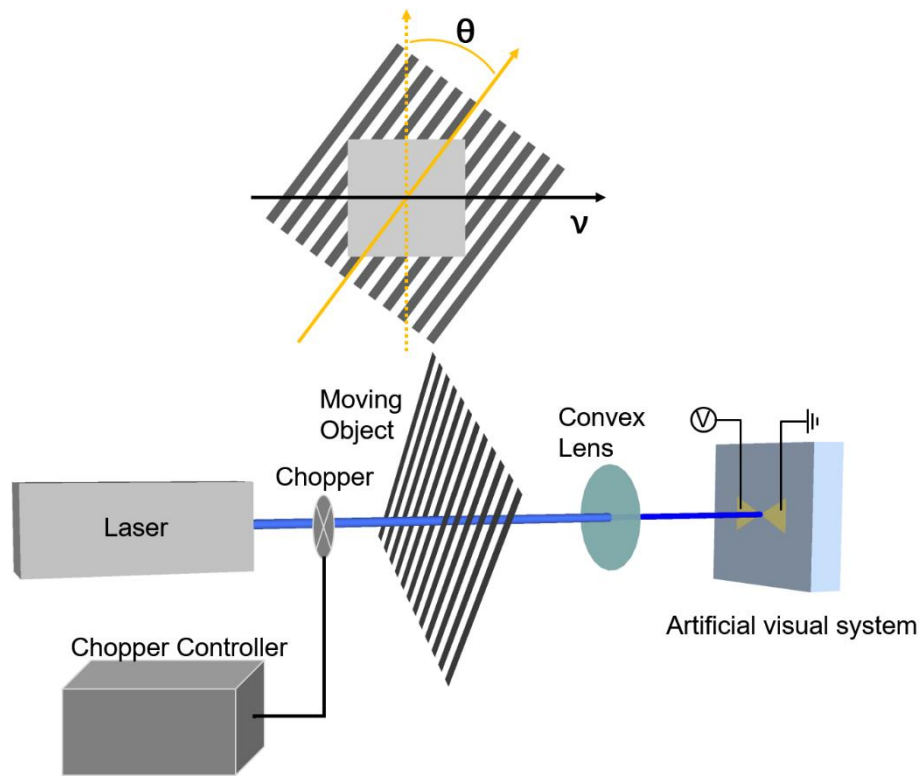
Fig. S19. Schematic diagram for the experimental setup of the "unattended" orientation selectivity.
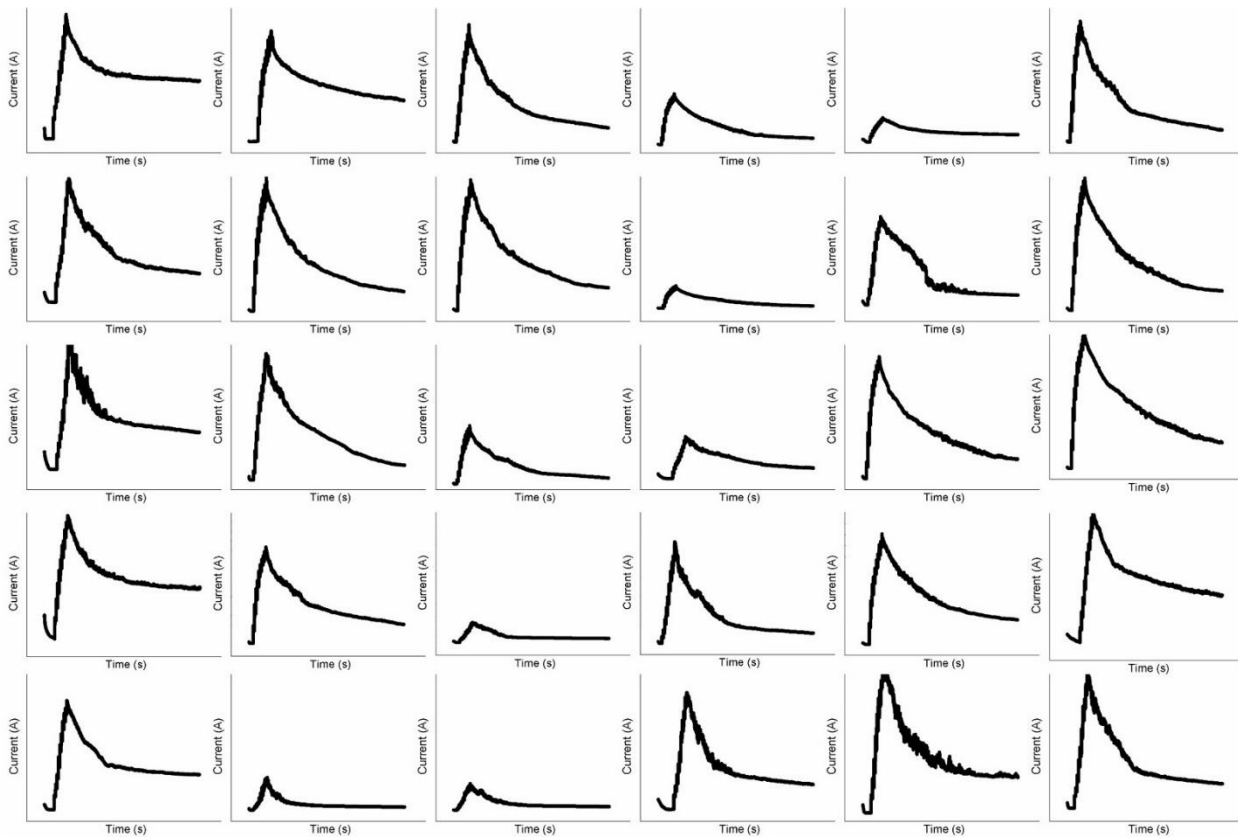
Fig. S20. Visual response of each pixel from the quasi-2DEGs artificial visual system that has 6 × 5 pixel arrays (total 30 devices).
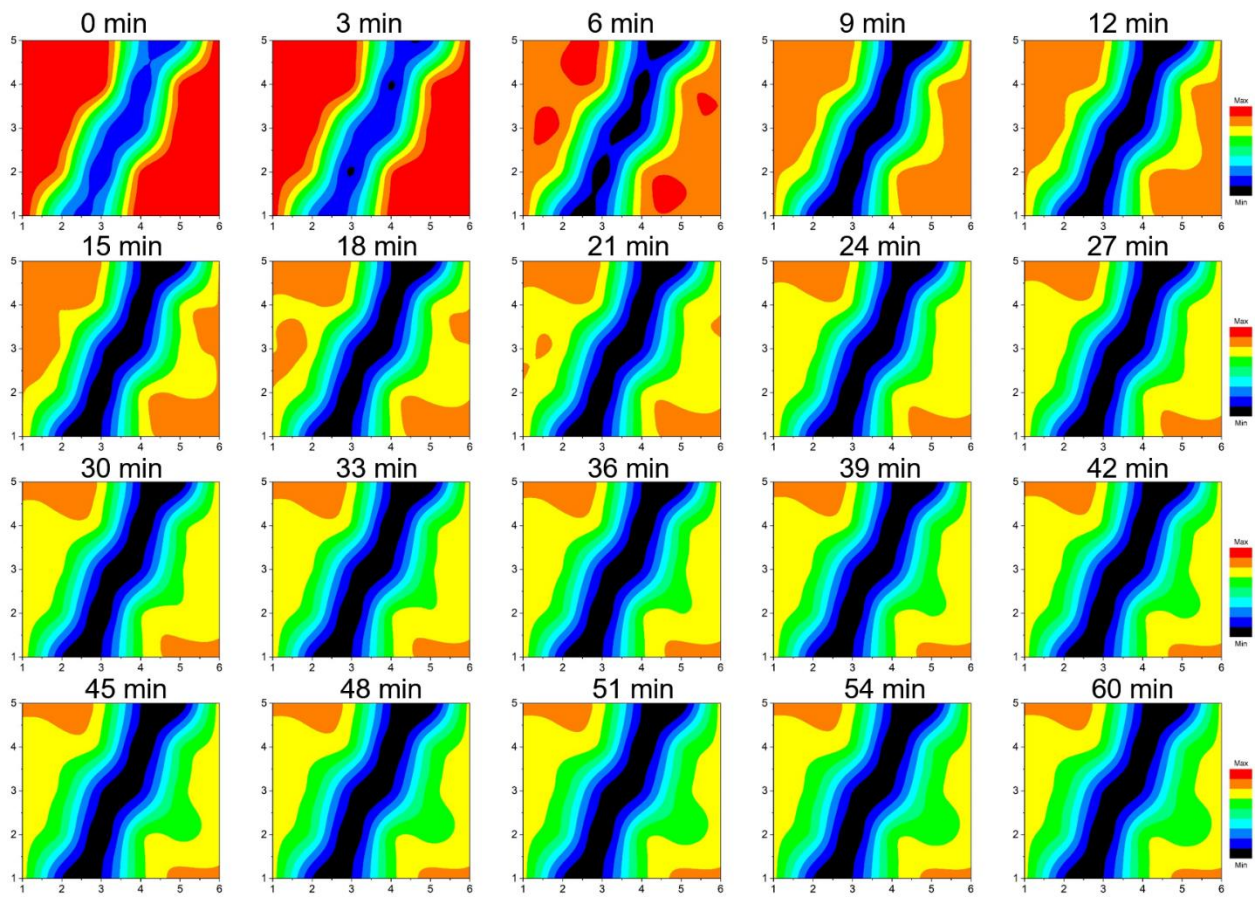
Fig. S21. Imaging and memorizing behaviors of the artificial visual system after different retention time.

1. Contact printing

2. Photoresist coating

3. Expose

4. Develop

5. Metal deposit

6. Lift off
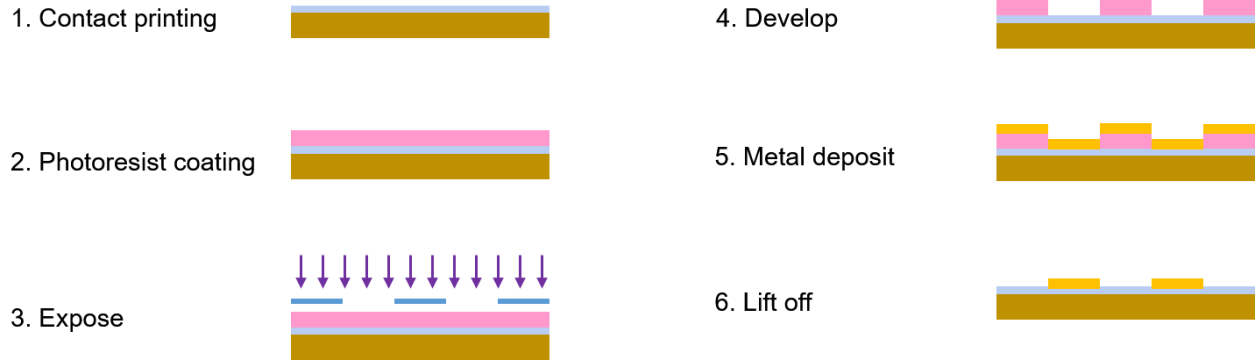
Fig. S22. Schematic illustration of the device fabrication process for artificial visual systems based on quasi-2DEGs photonic synapse arrays.

Table S1. Comparison of energy consumption of quasi-2DEGs photonic synapses with other state-of-the-art hardware-based artificial synapses.

Device	Active material	Energy consumption per spike (fJ)	Ref.
Electrolyte-gated transistor	Indium-zinc oxide thin film	45000	(*32*)
Electrolyte-gated transistor	Indium-zinc oxide thin film	3900	(*52*)
Electrolyte-gated transistor	PEO/P3HT core-sheath NWs	12.3 (10 NWs)	(*53*)
Dual-gate transistor	Single-walled CNT thin film	1000	(*54*)
Electrolyte-gated transistor	Multilayer MoO_3 nanoflake	9600	(*55*)
Electrolyte-gated transistor	Epitaxial WO_3 thin film	36000	(*56*)
Memristor	Conjugated polyelectrolyte film	10	(*57*)
Electrolyte-gated transistor	Multilayer WSe_2	30	(*58*)
Metal-insulator transition	Monolayer MoS_2	72	(*59*)
Dual-gated transistor	Indium-tungsten oxide thin film	9.3	(*60*)
Electrolyte-gated transistor	Multilayer MoS_2 nanoflake	4800	(*61*)
Photonic flash memory	Evaporated pentacene thin film	1400000	(*33*)
Quasi-2DEGs photonic synapses	$InGaO_3(ZnO)_3$ superlattice NWs	0.7 (30 NWs)	This work

Table S2. Comparison of photodetection performance of $InGaO_3(ZnO)_3$ superlattice NWs with other low dimensional semiconductor nanostructure-based photodetectors.

Photodetector	Responsivity (A/W)	Detectivity (Jones)	Ref.
CdS NW	2.6×10^5	2.3×10^{16}	(*62*)
ZnO NW	7×10^6	3.3×10^{17}	(*63*)
Graphene	1.5×10^3	1×10^{11}	(*64*)
Graphene/Ga_2O_3	39.3	5.9×10^{13}	(*65*)
MoS_2	10^4	7.7×10^{13}	(*66*)
MoS_2	7×10^4	3.5×10^{14}	(*67*)
WS_2	10^3	3.5×10^{11}	(*68*)
WSe_2/PbS QDs	2×10^5	1×10^{13}	(*69*)
WSe_2/SnS_2	244	1.29×10^{13}	(*70*)
PtS_2	1.56×10^6	2.9×10^{11}	(*71*)
$CsPbI_3$ NW	2920	5.17×10^{13}	(*72*)
$Cs_3Sb_2Cl_9$ NW	3616	1.25×10^6	(*73*)
$MAPbI_3$	410	9.1×10^{12}	(*74*)
$CsPbI_3$ NW	4489	7.9×10^{12}	(*30*)
$InGaO_3(ZnO)_3$ superlattice NW	1.05×10^6	3.15×10^{13}	This work

Table S3. Comparison of the maximum PPF index value of flexible quasi-2DEGs photonic synapses with state-of-the-art hardware-based artificial synapses.

Device	Active material	PPF index	Flexible?	Ref.
Electrolyte-gated transistor	Indium-zinc oxide thin film	180 %	No	(*32*)
Organic electrochemical transistor	PEDOT:PSS thin film	185 %	No	(*75*)
Electrolyte-gated transistor	PEO/P3HT core-sheath NWs	162 %	No	(*53*)
Electrolyte-gated transistor	Multilayer MoO_3 nanoflake	114 %	No	(*55*)
Organic field-effect transistors	P3HT thin film	190 %	No	(*76*)
Electrolyte-gated transistor	ZnO thin film	140 %	No	(*77*)
Organic electrochemical transistors	P3HT thin film	118 %	No	(*78*)
Memristor	Conjugated polyelectrolyte film	145 %	No	(*57*)
Photonic flash memory	Evaporated pentacene thin film	130 %	No	(*33*)
Electrolyte-gated transistor	Indium-tungsten oxide thin film	190 %	Yes	(*79*)
Memristor	Mesoporous silica	128 %	No	(*80*)
Quasi-2DEGs photonic synapses	$InGaO_3(ZnO)_3$ superlattice NWs	210 %	Yes	This work

Movie S1. Imaging and memorizing behaviors of the artificial visual system with different retention time.

REFERENCES AND NOTES

1. E. R. Kandel, J. H. Schwartz, T. M. Jessell, S. A. Siegelbaum, A. J. Hudspeth, *Principles of Neural Science* (McGraw-Hill New York, 2000).

2. L. F. Abbott, W. G. Regehr, Synaptic computation. *Nature* **431**, 796–803 (2004).

3. B. C.-K. Tee, A. Chortos, A. Berndt, A. K. Nguyen, A. Tom, A. M. Guire, Z. C. Lin, K. Tien, W.-G. Bae, H. Wang, P. Mei, H.-H. Chou, B. Cui, K. Deisseroth, T. N. Ng, Z. Bao, A skin-inspired organic digital mechanoreceptor. *Science* **350**, 313–316 (2015).

4. L. E. Osborn, A. Dragomir, J. L. Betthauser, C. L. Hunt, H. H. Nguyen, R. R. Kaliki, N. V. Thakor, Prosthesis with neuromorphic multilayered e-dermis perceives touch and pain. *Sci. Robot.* **3**, eaat3818 (2018).

5. Y. Kim, A. Chortos, W. Xu, Y. Liu, J. Y. Oh, D. Son, J. Kang, A. M. Foudeh, C. Zhu, Y. Lee, S. Niu, J. Liu, R. Pfattner, Z. Bao, T.-W. Lee, A bioinspired flexible organic artificial afferent nerve. *Science* **360**, 998–1003 (2018).

6. J. Mannhart, D. G. Schlom, Oxide interfaces–an opportunity for electronics. *Science* **327**, 1607–1611 (2010).

7. R. Ramesh, D. G. Schlom, Creating emergent phenomena in oxide superlattices. *Nat. Rev. Mater.* **4**, 257–268 (2019).

8. A. D. Caviglia, S. Gariglio, N. Reyren, D. Jaccard, T. Schneider, M. Gabay, S. Thiel, G. Hammerl, J. Mannhart, J.-M. Triscone, Electric field control of the $LaAlO_3/SrTiO_3$ interface ground state. *Nature* **456**, 624–627 (2008).

9. A. Tsukazaki, A. Ohtomo, T. Kita, Y. Ohno, H. Ohno, M. Kawasaki, Quantum hall effect in polar oxide heterostructures. *Science* **315**, 1388–1391 (2007).

10. A. Tsukazaki, S. Akasaka, K. Nakahara, Y. Ohno, H. Ohno, D. Maryenko, A. Ohtomo, M. Kawasaki, Observation of the fractional quantum Hall effect in an oxide. *Nat. Mater.* **9**, 889–893 (2010).

11. P. Irvin, Y. Ma, D. F. Bogorin, C. Cen, C. W. Bark, C. M. Folkman, C.-B. Eom, J. Levy, Rewritable nanoscale oxide photodetector. *Nat. Photonics* **4**, 849–852 (2010).

12. D. Miron, D. Cohen-Azarzar, B. Hoffer, M. Baskin, S. Kvatinsky, E. Yalon, L. Kornblum, Oxide 2D electron gases as a reservoir of defects for resistive switching. *Appl. Phys. Lett.* **116**, 223503 (2020).

13. H. Chen, Y. S. Rim, I. C. Wang, C. Li, B. Zhu, M. Sun, M. S. Goorsky, X. He, Y. Yang, Quasi-two-dimensional metal oxide semiconductors based ultrasensitive potentiometric biosensors. *ACS Nano* **11**, 4710–4718 (2017).

14. A. Tebano, E. Fabbri, D. Pergolesi, G. Balestrino, E. Traversa, Room-temperature giant persistent photoconductivity in $SrTiO_3/LaAlO_3$ heterostructures. *ACS Nano* **6**, 1278–1283 (2012).

15. B. Tian, C. M. Lieber, Nanowired bioelectric interfaces. *Chem. Rev.* **119**, 9136–9152 (2019).

16. F. Li, S. P. Yip, R. Dong, Z. Zhou, C. Lan, X. Liang, D. Li, Y. Meng, X. Kang, J. C. Ho, Crystalline InGaZnO quaternary nanowires with superlattice structure for high-performance thin-film transistors. *Nano Res.* **12**, 1796–1803 (2019).

17. F. Li, Y. Meng, R. Dong, S. P. Yip, C. Lan, X. Kang, F. Wang, K. S. Chan, J. C. Ho, High-performance transparent ultraviolet photodetectors based on InGaZnO superlattice nanowire arrays. *ACS Nano* **13**, 12042–12051 (2019).

18. H. Ohta, K. Nomura, M. Orita, M. Hirano, K. Ueda, T. Suzuki, Y. Ikuhara, H. Hosono, Single-crystalline films of the homologous series $InGaO_3(ZnO)_m$ grown by reactive solid-phase epitaxy. *Adv. Funct. Mater.* **13**, 139–144 (2003).

19. K. Nomura, H. Ohta, K. Ueda, T. Kamiya, M. Hirano, H. Hosono, Thin-film transistor fabricated in single-crystalline transparent oxide semiconductor. *Science* **300**, 1269–1272 (2003).

20. K. Nomura, H. Ohta, K. Ueda, T. Kamiya, M. Orita, M. Hirano, T. Suzuki, C. Honjyo, Y. Ikuhara, H. Hosono, Growth mechanism for single-crystalline thin film of $InGaO_3(ZnO)_5$ by reactive solid-phase epitaxy. *J. Appl. Phys.* **95**, 5532–5539 (2004).

21. D. L. Huang, L. L. Wu, X. T. Zhang, Size-Dependent InAlO$_3$(ZnO)$_m$ nanowires with a perfect superlattice structure. *J. Phys. Chem. C* **114**, 11783–11786 (2010).

22. H. Faber, S. Das, Y.-H. Lin, N. Pliatsikas, K. Zhao, T. Kehagias, G. Dimitrakopulos, A. Amassian, P. A. Patsalas, T. D. Anthopoulos, Heterojunction oxide thin-film transistors with unprecedented electron mobility grown from solution. *Sci. Adv.* **3**, e1602640 (2017).

23. J. Z. Li, J. Y. Lin, H. X. Jiang, M. Asif Khan, Q. Chen, Persistent photoconductivity in a two-dimensional electron gas system formed by an AlGaN/GaN heterostructure. *J. Appl. Phys.* **82**, 1227–1230 (1997).

24. N. Han, F. Wang, J. J. Hou, S. P. Yip, H. Lin, F. Xiu, M. Fang, Z. Yang, X. Shi, G. Dong, T. F. Hung, J. C. Ho, Tunable electronic transport properties of metal-cluster-decorated III-V nanowire transistors. *Adv. Mater.* **25**, 4445–4451 (2013).

25. Z. Shao, T. Jiang, X. Zhang, X. Zhang, X. Wu, F. Xia, S. Xiong, S.-T. Lee, J. Jie, Memory phototransistors based on exponential-association photoelectric conversion law. *Nat. Commun.* **10**, 1294 (2019).

26. W. Meevasana, P. D. C. King, R. H. He, S-K. Mo, M. Hashimoto, A. Tamai, P. Songsiriritthigul, F. Baumberger, Z.-X. Shen, Creation and control of a two-dimensional electron liquid at the bare SrTiO$_3$ surface. *Nat. Mater.* **10**, 114–118 (2011).

27. W. Gerstner, W. M. Kistler, *Spiking Neuron Models: Single Neurons*, *Populations*, *Plasticity* (Cambridge Univ. Press, 2002).

28. D. Kuzum, S. Yu, H.-S. Philip Wong, Synaptic electronics: Materials, devices and applications. *Nanotechnology* **24**, 382001 (2013).

29. J. Park, M.-W. Kwon, H. Kim, S. Hwang, J.-J. Lee, B.-G. Park, Compact neuromorphic system with four-terminal si-based synaptic devices for spiking neural networks. *IEEE Trans. Electron Devices* **64**, 2438–2444 (2017).

30. Y. Meng, C. Lan, F. Li, S. P. Yip, R. Wei, X. Kang, X. Bu, R. Dong, H. Zhang, J. C. Ho, Direct vapor-liquid-solid synthesis of all-inorganic perovskite nanowires for high-performance electronics and optoelectronics. *ACS Nano* **13**, 6060–6070 (2019).

31. S. Thiel, G. Hammerl, A. Schmehl, C. W. Schneider, J. Mannhart, Tunable quasi-two-dimensional electron gases in oxide heterostructures. *Science* **313**, 1942–1945 (2006).

32. L. Q. Zhu, C. J. Wan, L. Q. Guo, Y. Shi, Q. Wan, Artificial synapse network on inorganic proton conductor for neuromorphic systems. *Nat. Commun.* **5**, 3158 (2014).

33. Y. Wang, Z. Lv, J. Chen, Z. Wang, Y. Zhou, L. Zhou, X. Chen, S.-T. Han, Photonic synapses based on inorganic perovskite quantum dots for neuromorphic computing. *Adv. Mater.* **30**, 1802883 (2018).

34. B. Pradhan, S. Das, J. Li, F. Chowdhury, J. Cherusseri, D. Pandey, D. Dev, A. Krishnaprasad, E. Barrios, A. Towers, A. Gesquiere, L. Tetard, T. Roy, J. Thomas, Ultrasensitive and ultrathin phototransistors and photonic synapses using perovskite quantum dots grown from graphene lattice. *Sci. Adv.* **6**, eaay5225 (2020).

35. F.-S. Yang, M. Li, M.-P. Lee, I-Y. Ho, J.-Y. Chen, H. Ling, Y. Li, J.-K. Chang, S.-H. Yang, Y.-M. Chang, K.-C. Lee, Y.-C. Chou, C.-H. Ho, W. Li, C.-H. Lien, Y.-F. Lin, Oxidation-boosted charge trapping in ultra-sensitive van der Waals materials for artificial synaptic features. *Nat. Commun.* **11**, 2972 (2020).

36. T. Chang, S.-H. Jo, W. Lu, Short-term memory to long-term memory transition in a nanoscale memristor. *ACS Nano* **5**, 7669–7676 (2011).

37. S. Gao, G. Liu, H. Yang, C. Hu, Q. Chen, G. Gong, W. Xue, X. Yi, J. Shang, R.-W. Li, An oxide Schottky junction artificial optoelectronic synapse. *ACS Nano* **13**, 2634–2642 (2019).

38. K. L. Magleby, The effect of repetitive stimulation on facilitation of transmitter release at the frog neuromuscular junction. *J. Physiol.* **234**, 327–352 (1973).

39. R. Shapley, M. Hawken, D. L. Ringach, Dynamics of orientation selectivity in the primary visual cortex and the importance of cortical inhibition. *Neuron* **38**, 689–699 (2003).

40. W. S. Geisler, D. G. Albrecht, Visual cortex neurons in monkeys and cats: Detection, discrimination, and identification. *Vis. Neurosci.* **14**, 897–919 (1997).

41. C. J. McAdams, J. H. R. Maunsell, Effects of attention on orientation-tuning functions of single neurons in macaque cortical area V4. *J. Neurosci.* **19**, 431–441 (1999).

42. S. Yu, B. Gao, Z. Fang, H. Yu, J. Kang, H.-S. P. Wong, A low energy oxide-based electronic synaptic device for neuromorphic visual systems with tolerance to device variation. *Adv. Mater.* **25**, 1774–1779 (2013).

43. C. J. Wan, L. Q. Zhu, Y. H. Liu, P. Feng, Z. P. Liu, H. L. Cao, P. Xiao, Y. Shi, Q. Wan, Proton-conducting graphene oxide-coupled neuron transistors for brain-inspired cognitive systems. *Adv. Mater.* **28**, 3557–3563 (2016).

44. Z. Wang, T. Zeng, Y. Ren, Y. Lin, H. Xu, X. Zhao, Y. Liu, D. Ielmini, Toward a generalized Bienenstock-Cooper-Munro rule for spatiotemporal learning via triplet-STDP in memristive devices. *Nat. Commun.* **11**, 1510 (2020).

45. F. Zhou, Z. Zhou, J. Chen, T. H. Choy, J. Wang, N. Zhang, Z. Lin, S. Yu, J. Kang, H.-S. P. Wong, Y. Chai, Optoelectronic resistive random access memory for neuromorphic vision sensors. *Nat. Nanotechnol.* **14**, 776–782 (2019).

46. S. Chen, Z. Lou, D. Chen, G. Shen, An artificial flexible visual memory system based on an UV-motivated Memristor. *Adv. Mater.* **30**, 1705400 (2018).

47. W. Kim, A. Javey, O. Vermesh, Q. Wang, Y. Li, H. Dai, Hysteresis caused by water molecules in carbon nanotube field-effect transistors. *Nano Lett.* **3**, 193–198 (2003).

48. J. K. Jeong, H. Won Yang, J. H. Jeong, Y.-G. Mo, H. D. Kim, Origin of threshold voltage instability in indium-gallium-zinc oxide thin film transistors. *Appl. Phys. Lett.* **93**, 123508 (2008).

49. J.-S. Park, J. K. Jeong, H.-J. Chung, Y.-G. Mo, H. D. Kim, Electronic transport properties of amorphous indium-gallium-zinc oxide semiconductor upon exposure to water. *Appl. Phys. Lett.* **92**, 072104 (2008).

50. P.-T. Liu, Y.-T. Chou, L.-F. Teng, Environment-dependent metastability of passivation-free indium zinc oxide thin film transistor after gate bias stress. *Appl. Phys. Lett.* **95**, 233504 (2009).

51. E. Di Gennaro, U. S. di Uccio, C. Aruta, C. Cantoni, A. Gadaleta, A. R. Lupini, D. Maccariello, D. Marré, I. Pallecchi, D. Paparo, P. Perna, M. Riaz, F. M. Granozio, Persistent photoconductivity in 2D electron gases at different oxide interfaces. *Adv. Opt. Mater.* **1**, 834–843 (2013).

52. Y. H. Liu, L. Q. Zhu, P. Feng, Y. Shi, Q. Wan, Freestanding artificial synapses based on laterally proton-coupled transistors on chitosan membranes. *Adv. Mater.* **27**, 5599–5604 (2015).

53. W. Xu, S.-Y. Min, H. Hwang, T.-W. Lee, Organic core-sheath nanowire artificial synapses with femtojoule energy consumption. *Sci. Adv.* **2**, e1501326 (2016).

54. P. Feng, W. W. Xu, Y. Yang, X. Wan, Y. Shi, Q. Wan, J. W. Zhao, Z. Cui, Printed neuromorphic devices based on printed carbon nanotube thin-film transistors. *Adv. Funct. Mater.* **27**, 1604447 (2017).

55. C. S. Yang, D. S. Shang, N. Liu, G. Shi, X. Shen, R. C. Yu, Y. Q. Li, Y. Sun, A synaptic transistor based on Quasi-2D molybdenum oxide. *Adv. Mater.* **29**, 1700906 (2017).

56. J.-T. Yang, C. Ge, J.-Y. Du, H.-Y. Huang, M. He, C. Wang, H.-B. Lu, G.-Z. Yang, K.-J. Jin, Artificial synapses emulated by an electrolyte-gated tungsten-oxide transistor. *Adv. Mater.*, 1801548 (2018).

57. W. Xu, T. L. Nguyen, Y.-T. Kim, C. Wolf, R. Pfattner, J. Lopez, B.-G. Chae, S.-I. Kim, M. Y. Lee, E.-Y. Shin, Y.-Y. Noh, J. H. Oh, H. Hwang, C.-G. Park, H. Y. Woo, T.-W. Lee, Ultrasensitive artificial synapse based on conjugated polyelectrolyte. *Nano Energy* **48**, 575–581 (2018).

58. J. Zhu, Y. Yang, R. Jia, Z. Liang, W. Zhu, Z. U. Rehman, L. Bao, X. Zhang, Y. Cai, L. Song, R. Huang, Ion gated synaptic transistors based on 2D van der waals crystals with tunable diffusive dynamics. *Adv. Mater.* **30**, 1800195 (2018).

59. L. Sun, Y. Zhang, G. Hwang, J. Jiang, D. Kim, Y. A. Eshete, R. Zhao, H. Yang, Synaptic computation enabled by joule heating of single-layered semiconductors for sound localization. *Nano Lett.* **18**, 3229–3234 (2018).

60. R. A. John, N. Tiwari, C. Yaoyi, Ankit, N. Tiwari, M. Kulkarni, A. Nirmal, A. C. Nguyen, A. Basu, N. Mathews, Ultralow power dual-gated subthreshold oxide neuristors: An enabler for higher order neuronal temporal correlations. *ACS Nano* **12**, 11263–11273 (2018).

61. R. A. John, F. Liu, N. A. Chien, M. R. Kulkarni, C. Zhu, Q. Fu, A. Basu, Z. Liu, N. Mathews, Synergistic gating of electro-iono-photoactive 2D chalcogenide neuristors: Coexistence of hebbian and homeostatic synaptic metaplasticity. *Adv. Mater.* **30**, 1800220 (2018).

62. D. Zheng, H. Fang, P. Wang, W. Luo, F. Gong, J. C. Ho, X. Chen, W. Lu, L. Liao, J. Wang, High-Performance ferroelectric polymer side-gated CdS nanowire ultraviolet photodetectors. *Adv. Funct. Mater.* **26**, 7690–7696 (2016).

63. X. Liu, L. Gu, Q. Zhang, J. Wu, Y. Long, Z. Fan, All-printable band-edge modulated ZnO nanowire photodetectors with ultra-high detectivity. *Nat. Commun.* **5**, 4007 (2014).

64. C.-H. Liu, Y.-C. Chang, T. B. Norris, Z. H. Zhong, Graphene photodetectors with ultra-broadband and high responsivity at room temperature. *Nat. Nanotechnol.* **9**, 273–278 (2014).

65. W.-Y. Kong, G.-A. Wu, K.-Y. Wang, T.-F. Zhang, Y.-F. Zou, D.-D. Wang, L.-B. Luo, Graphene-β-Ga_2O_3 heterojunction for highly sensitive deep UV photodetector application. *Adv. Mater.* **28**, 10725–10731 (2016).

66. D. Kufer, G. Konstantatos, Highly sensitive, encapsulated MoS_2 photodetector with gate controllable gain and speed. *Nano Lett.* **15**, 7307–7313 (2015).

67. N. Huo, G. Konstantatos, Ultrasensitive all-2D MoS_2 phototransistors enabled by an out-of-plane MoS_2 PN homojunction. *Nat. Commun.* **8**, 572 (2017).

68. F. Gong, W. Luo, J. Wang, P. Wang, H. Fang, D. Zheng, N. Guo, J. Wang, M. Luo, J. C. Ho, X. Chen, W. Lu, L. Liao, W. Hu, High-sensitivity floating-gate phototransistors based on WS_2 and MoS_2. *Adv. Funct. Mater.* **26**, 6084–6090 (2016).

69. C. Hu, D. Dong, X. Yang, K. Qiao, D. Yang, H. Deng, S. Yuan, J. Khan, Y. Lan, H. Song, J. Tang, Synergistic effect of hybrid PbS quantum Dots/2D-WSe_2 toward high performance and broadband phototransistors. *Adv. Funct. Mater.* **27**, 1603605 (2017).

70. X. Zhou, X. Hu, S. Zhou, H. Song, Q. Zhang, L. Pi, L. Li, H. Li, J. Lü, T. Zhai, Tunneling diode based on WSe_2/SnS_2 heterostructure incorporating high detectivity and responsivity. *Adv. Mater.* **30**, 1703286 (2018).

71. L. Li, W. Wang, Y. Chai, H. Li, M. Tian, T. Zhai, Few-Layered PtS_2 Phototransistor on h-BN with High Gain. *Adv. Funct. Mater.* **27**, 1701011 (2017).

72. T. Yang, Y. Zheng, Z. Du, W. Liu, Z. Yang, F. Gao, L. Wang, K.-C. Chou, X. Hou, W. Yang, Superior photodetectors based on all-inorganic perovskite $CsPbI_3$ nanorods with ultrafast response and high stability. *ACS Nano* **12**, 1611–1617 (2018).

73. B. Pradhan, G. S. Kumar, S. Sain, A. Dalui, U. K. Ghorai, S. K. Pradhan, S. Acharya, Size tunable cesium antimony chloride perovskite nanowires and nanorods. *Chem. Mater.* **30**, 2135–2142 (2018).

74. Q. Zhou, J. G. Park, R. Nie, A. K. Thokchom, D. Ha, J. Pan, S. I. Seok, T. Kim, Nanochannel-assisted perovskite nanowires: From growth mechanisms to photodetector applications. *ACS Nano* **12**, 8406–8414 (2018).

75. P. Gkoupidenis, N. Schaefer, B. Garlan, G. G. Malliaras, Neuromorphic functions in PEDOT:PSS organic electrochemical transistors. *Adv. Mater.* **27**, 7176–7180 (2015).

76. Y. Zang, H. Shen, D. Huang, C.-A. Di, D. Zhu, A dual-organic-transistor-based tactile-perception system with signal-processing functionality. *Adv. Mater.* **29**, 1606088 (2017).

77. R. A. John, J. Ko, M. R. Kulkarni, N. Tiwari, N. A. Chien, N. G. Ing, W. L. Leong, N. Mathews, Flexible ionic-electronic hybrid oxide synaptic TFTs with programmable dynamic plasticity for brain-inspired neuromorphic computing. *Small* **13**, 1701193 (2017).

78. L.-a. Kong, J. Sun, C. Qian, Y. Fu, J. X. Wang, J. L. Yang, Y. L. Gao, Long-term synaptic plasticity simulated in ionic liquid/polymer hybrid electrolyte gated organic transistors. *Org. Electron.* **47**, 126–132 (2017).

79. C. Wan, G. Chen, Y. Fu, M. Wang, N. Matsuhisa, S. Pan, L. Pan, H. Yang, Q. Wan, L. Zhu, X. Chen, An artificial sensory neuron with tactile perceptual learning. *Adv. Mater.* **30**, 1801291 (2018).

80. B. Li, Y. Liu, C. Wan, Z. Liu, M. Wang, D. Qi, J. Yu, P. Cai, M. Xiao, Y. Zeng, X. Chen, Mediating short-term plasticity in an artificial memristive synapse by the orientation of silica mesopores. *Adv. Mater.* **30**, 1706395 (2018).